

Optical and structural characterization of iron oxide and cobalt oxide thin films at 800 nm

Hans A. Garcia · Ronaldo P. de Melo Jr. ·
Antonio Azevedo · Cid B. de Araújo

Received: 25 December 2012 / Accepted: 9 January 2013 / Published online: 30 January 2013
© Springer-Verlag Berlin Heidelberg 2013

Abstract We report on optical and structural properties of α -Fe₂O₃ and Co₃O₄ thin films, grown by direct oxidation of pure metal films deposited on soda-lime glass. Structural characteristics and morphology of the films were investigated by X-ray diffraction, atomic force microscopy, and scanning electron microscopy. Linear optical absorption, and linear refraction as well as non-linear optical properties were investigated. The third-order optical susceptibilities were measured applying the *Thermally managed Z-scan technique* using a Ti: sapphire laser (150 fs; 800 nm). The results obtained for the Co₃O₄ film were $\text{Re}\chi^{(3)} = -(5.7 \pm 2.4) \times 10^{-9}$ esu and $\text{Im}\chi^{(3)} = -(1.8 \pm 0.2) \times 10^{-8}$ esu while for the α -Fe₂O₃ film we determined $\text{Re}\chi^{(3)} = +(6.6 \pm 2.4) \times 10^{-10}$ esu and $\text{Im}\chi^{(3)} = +(2.2 \pm 0.4) \times 10^{-10}$ esu.

1 Introduction

Transition-metal oxides (TMO) exhibit a variety of interesting properties that can be exploited for applications such as magnetic storage, gas sensing, photonics and

biomedicine [1–3]. The increasing interest in these materials has driven the search for reliable fabrication techniques of high-quality thin films and nanoparticles in the last decade [4–14]. In particular, straightforward synthesis of single crystalline phase TMO films has been a long-standing issue because these materials exhibit many stoichiometric forms. Besides the conventional applications, TMO are suitable for bottom-up fabrication of self-assembled nanostructures and offer large variety of opportunities for physical as well for technological applications.

Our interest in TMO films is mainly justified by their large nonlinear (NL) optical properties that depend on the chemical nature of the constituents and the crystalline structure. These materials present high third-order optical susceptibility, $\chi^{(3)}$, that makes them very attractive for photonic applications. For instance, Ando et al. [15] showed that films of Co₃O₄, Fe₂O₃, V₂O₅, CuO, Mn₃O₄, NiO and Cr₂O₃ present NL susceptibilities larger than $\approx 10^{-9}$ esu. The phase-conjugation experiments of [15] were performed using lasers with pulse duration of 7 ns and 35 ps. Hashimoto et al. [16] studied sol-gel derived iron oxide films using the third-harmonic generation technique with a laser operating at 1,900 nm and measured NL susceptibilities between 10^{-11} and 10^{-10} esu. More recent reports of the NL properties of TMO films and nanoparticles [17–21] describe experiments with pulsed lasers that indicate a large potential of these materials for NL photonics.

Among the TMO, iron oxide and cobalt oxide deserve special attention because of their high NL response and their large thermal and chemical stabilities. It is known that while cobalt oxide typically crystallizes in two stable phases (CoO and Co₃O₄) [1], iron oxide crystallizes in many phases, such as magnetite (Fe₃O₄), hematite

H. A. Garcia · A. Azevedo · C. B. de Araújo (✉)
Departamento de Física, Universidade Federal de Pernambuco,
Recife, PE 50670-901, Brazil
e-mail: cid@df.ufpe.br

R. P. de Melo Jr.
Programa de Pós-Graduação em Ciência de Materiais,
Universidade Federal de Pernambuco, Recife, PE 50670-901,
Brazil

R. P. de Melo Jr.
Colegio Militar do Recife Exército Brasileiro, Recife,
PE 50730-120, Brazil

(α -Fe₂O₃), maghemite (γ -Fe₂O₃) and wurtzite (FeO) [2]. Besides being used for magnetic applications, Co₃O₄ has been considered for photonic devices such as optical limiters [21, 22]. On the other hand, Fe₂O₃ is a material of relatively small band gap and has been used in photochromic [4], optical limiting [23] and electrochromic [24] devices. In addition, nonstoichiometric films of iron oxide have been employed as gas sensors [25] and solar cells [26] by several years.

Unfortunately, most of the published papers on the NL properties of the iron oxide and cobalt oxide films do not provide enough information on the structural characteristics of the samples used although this is very important since the NL response of both materials is dependent on their stoichiometric form and crystalline structure. Also, the near-infrared NL response of iron oxide and cobalt oxide thin films were not investigated in details.

In the present article, we report on our investigation of the NL optical characteristics of iron oxide and cobalt oxide thin films prepared by direct oxidation of pure metal films. We describe the films preparation, the structural and optical properties of the samples and present measurements of the NL refractive index, n_2 , and the NL absorption coefficient, α_2 , at 800 nm.

The paper is organized as follows: the fabrication procedure and the techniques used to characterize the samples are described in Sect. 2. In Sect. 3 we present the structural characterization of the films and report on the linear and NL optical properties of the samples together with a discussion about the origin of the optical response. Finally in Sect. 4, we present a summary of the results.

2 Experimental details

Initially Fe and Co films were produced by thermal evaporation of high-purity metal chips on substrates of soda-lime glass with 1.0 mm thickness in a vacuum chamber with base pressure of 3.5×10^{-6} torr. The oxidation process was carried out at 400 °C in the presence of a high-purity oxygen flux (50 sccm) during time intervals varying from few minutes to several hours. By using this method we investigated the film growth dynamics as a function of the oxidation time. After each oxidation stage the film thickness was determined using a profilometer by measuring the step-height between the substrate and the top of the deposited layer.

The structural analysis of the films was carried out by X-ray diffraction (XRD) using the CuK α radiation at 1.5406 Å. The surface morphology of the samples was investigated by using a scanning electron microscope (SEM) and an atomic force microscope (AFM).

The linear optical absorption spectra of the samples were obtained using a commercial spectrophotometer and the linear refractive indices were measured using the prism-coupler technique. The NL measurements were performed applying the thermally managed Z-scan (TM-Z scan) technique [27–30] using a mode-locked Ti:sapphire laser (150 fs, 800 nm, 76 MHz).

3 Results and discussion

3.1 X-ray diffraction and AFM measurements

The samples' thickness was controlled during the oxidation process. Initially the thickness of the iron film was 100 nm and after 1 h of oxidation the film thickness reaches the saturation value of 200 nm. In the cobalt oxide case we started with a film having thickness of 32 nm and after 2 h of oxidation the thickness reached the saturation value of 70 nm. This procedure was repeated for many samples in order to assure that all analyzed films were completely oxidized.

XRD patterns of the films for different annealing times are shown in Fig. 1. Since the pure iron films are very

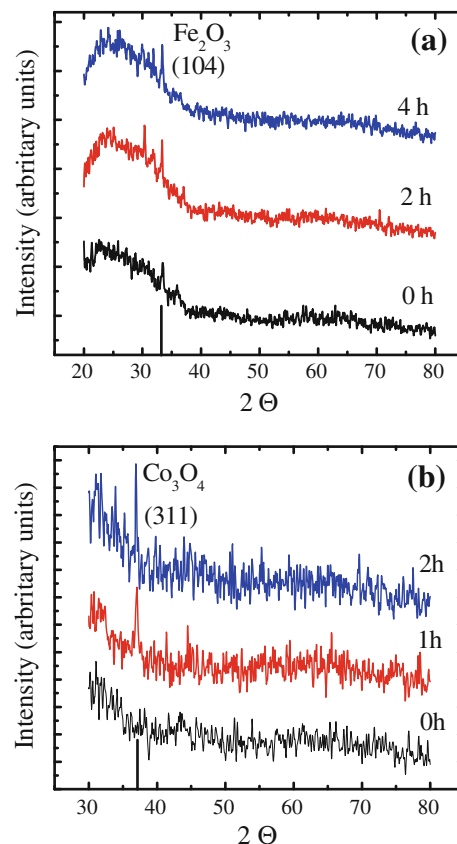


Fig. 1 X-ray diffraction patterns of the thin films: **a** iron oxide; **b** cobalt oxide

reactive in air, the as-deposited films present a XRD pattern that indicates the presence of Fe₂O₃. After annealing at 400 °C the XRD pattern exhibited a diffraction peak at $2\theta = 33.18^\circ$ corresponding to crystalline hematite (α -Fe₂O₃) as illustrated in Fig. 1a. Indeed diffraction peaks corresponding to α -Fe₂O₃ were seen even after few minutes of oxidation. Figure 1b shows the XRD pattern for a 70-nm-thick cobalt oxide film. As the initial thickness of pure cobalt film is very thin (32 nm), the corresponding peaks are not easily seen in the XRD data. The pattern corresponding to Co₃O₄, observed after the oxidation process is complete, corresponds to the (311) plane of Co₃O₄ with a diffraction peak at $2\theta = 36.88^\circ$.

Figure 2a shows results of the AFM measurements for a 200-nm-thick α -Fe₂O₃ film that presents a surface roughness with root-mean-square (rms) of 8.1 nm. This is due to the vertical nanostructures that grew on top of the film during the annealing process, as observed in Fig. 2b. Most of the self-assembled vertical structures exhibit wire and blade shapes as in [31].

Figure 3a shows an AFM image of a 55-nm-thick pure cobalt film with a rms surface roughness of 0.84 nm. Figure 3b shows the histogram of particle sizes with an average diameter of 2.5 nm. Figure 3c, d shows a representative AFM image and a histogram of the particle sizes for a Co₃O₄ film, respectively. The cobalt oxide film of 70 nm thickness, exhibits a surface roughness with rms of

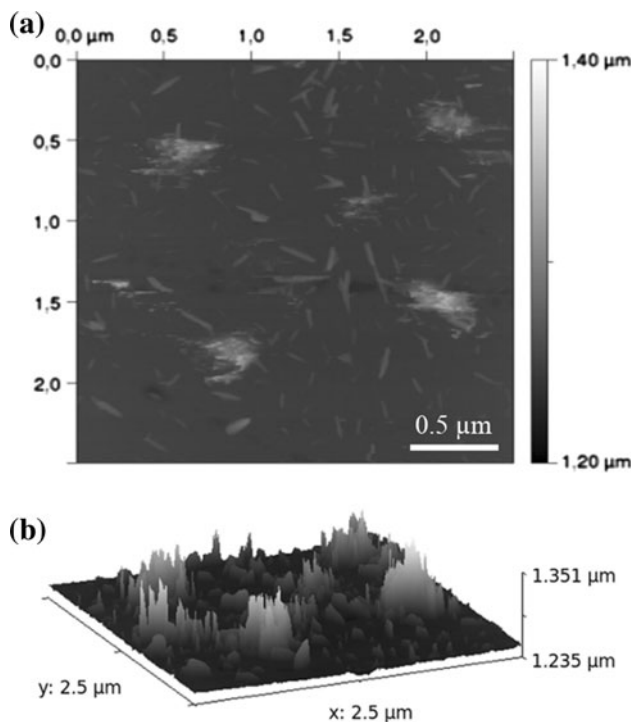


Fig. 2 AFM images of the iron oxide film surface showing the vertical nanostructures that grow on top of the film during the oxidation process

11.4 nm; the average particle size is 25 nm that is larger than the average particle size observed in the pure Co film. The SEM image, with magnification of 60×10^3 times, shows rod-shaped structures as illustrated in Fig. 3e. The cobalt oxide films did not present the spontaneous self-assembly of vertical nanostructures observed in the α -Fe₂O₃ films.

3.2 Linear optical absorption measurements

The optical transmittance spectra of films annealed during different times are shown in Fig. 4. Notice that for both materials the transmission increases for longer annealing times due to the oxidation process. As illustrated in Fig. 4a, the α -Fe₂O₃ films annealed at 400 °C during 60 min are completely oxidized and present a transmittance larger than 80 % (without correction for Fresnel reflections) in the red and near-infrared regions. Figure 4b shows that the Co₃O₄ films exhibit low optical transmittance from 300 to 500 nm. Their transmittances increase for wavelengths larger than 500 nm reaching a maximum around 620 nm and again decrease to a minimum transmission at ≈ 750 nm. At 800 nm a transmittance of ≈ 25 % is observed.

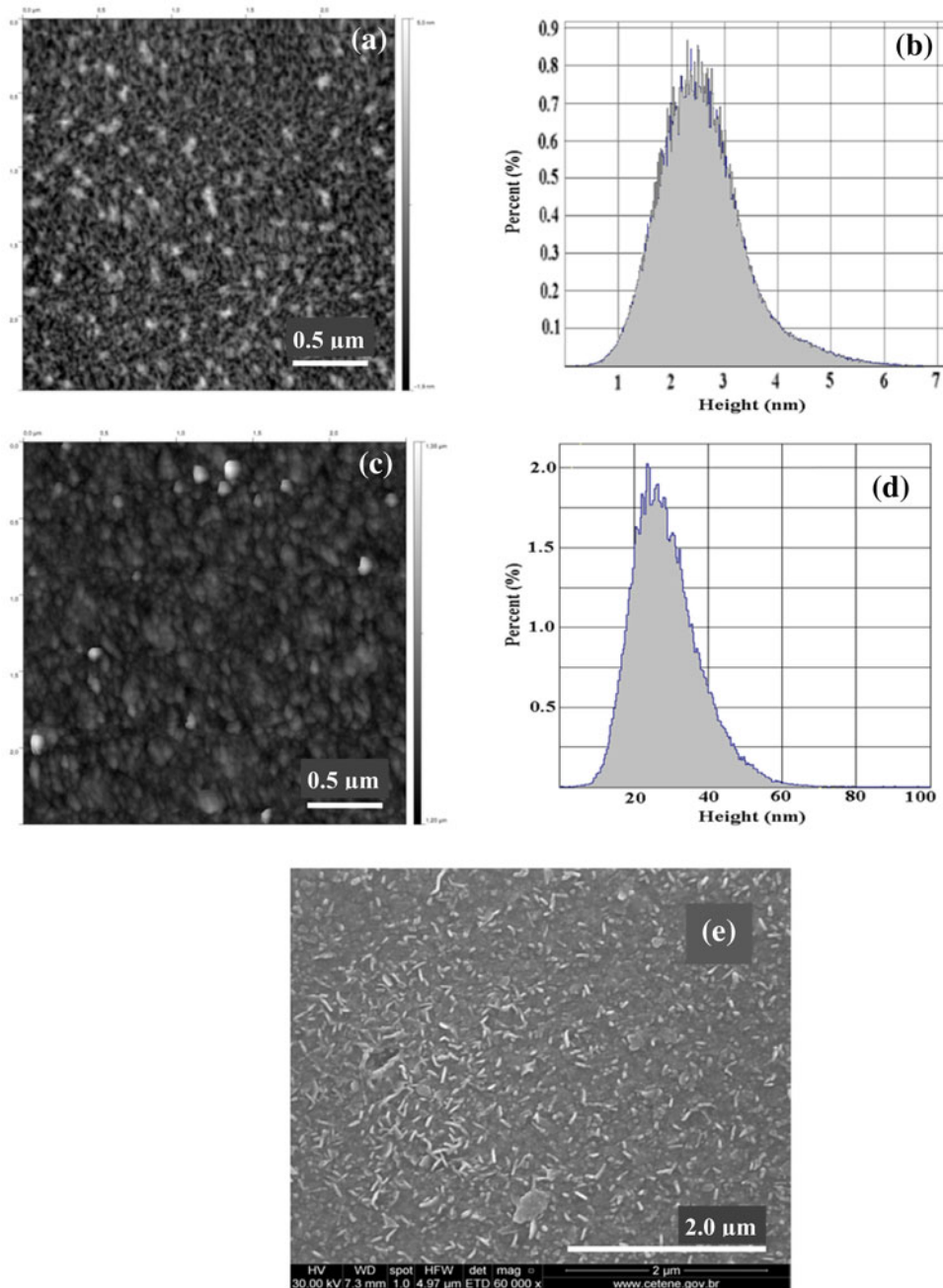
Figure 4c, d shows the wavelength dependence of the linear absorption coefficient, α_0 , of the samples used in the NL experiments.

The spectrum of α -Fe₂O₃ is well understood and according to [10] the absorption for wavelengths shorter than 400 nm is attributed to ligand-to-metal charge transfer transitions. In the region from 400 to 600 nm the spectrum is associated to $3d$ - $3d$ electronic transitions, double-exciton process involving a pair of Fe³⁺ ions, and charge transfer transitions. From 600 to 800 nm the origin of the absorption is related to $3d$ - $3d$ transitions [10].

The Co₃O₄ films exhibit absorption bands in the infrared-visible range associated to d -states of the Co²⁺ and Co³⁺ ions that occupy octahedral and tetrahedral symmetry sites, respectively [32, 33]. The absorption band centered at ≈ 410 nm (≈ 3.04 eV) is due to the charge transfer transition $p(O^{2-}) \rightarrow e_g(Co^{3+})$ while the band centered at ≈ 750 nm (≈ 1.66 eV) is ascribed to transitions associated to d -electrons of the Co³⁺ and Co²⁺ ions. The valence-to-conduction-band transition corresponds to the bandgap of 2.22 eV (561 nm), while transitions below the conduction band have been attributed the presence of Co⁺³ that gives rise to sub-band in the energy gap [32].

The dependence of α_0^2 as a function of the photon energy is shown in Fig. 4e, f. The optical band gap energy, E_g , for both samples was obtained by extrapolation of the linear portion of the data toward the energy axis. The intercept of the straight line for the α -Fe₂O₃ film shows that $E_g = 2.3$ eV (≈ 541 nm) while the Co₃O₄ sample presents two band gaps of direct allowed transitions, one band gap

Fig. 3 **a** AFM image and **b** the histogram for the particle size distribution for the as-deposited Co film. **c** AFM image and **d** histogram for particle size distribution for the Co_3O_4 film. **e** SEM image for a Co_3O_4 film after annealing exposed to oxygen atmosphere (image magnification: 60×10^3)

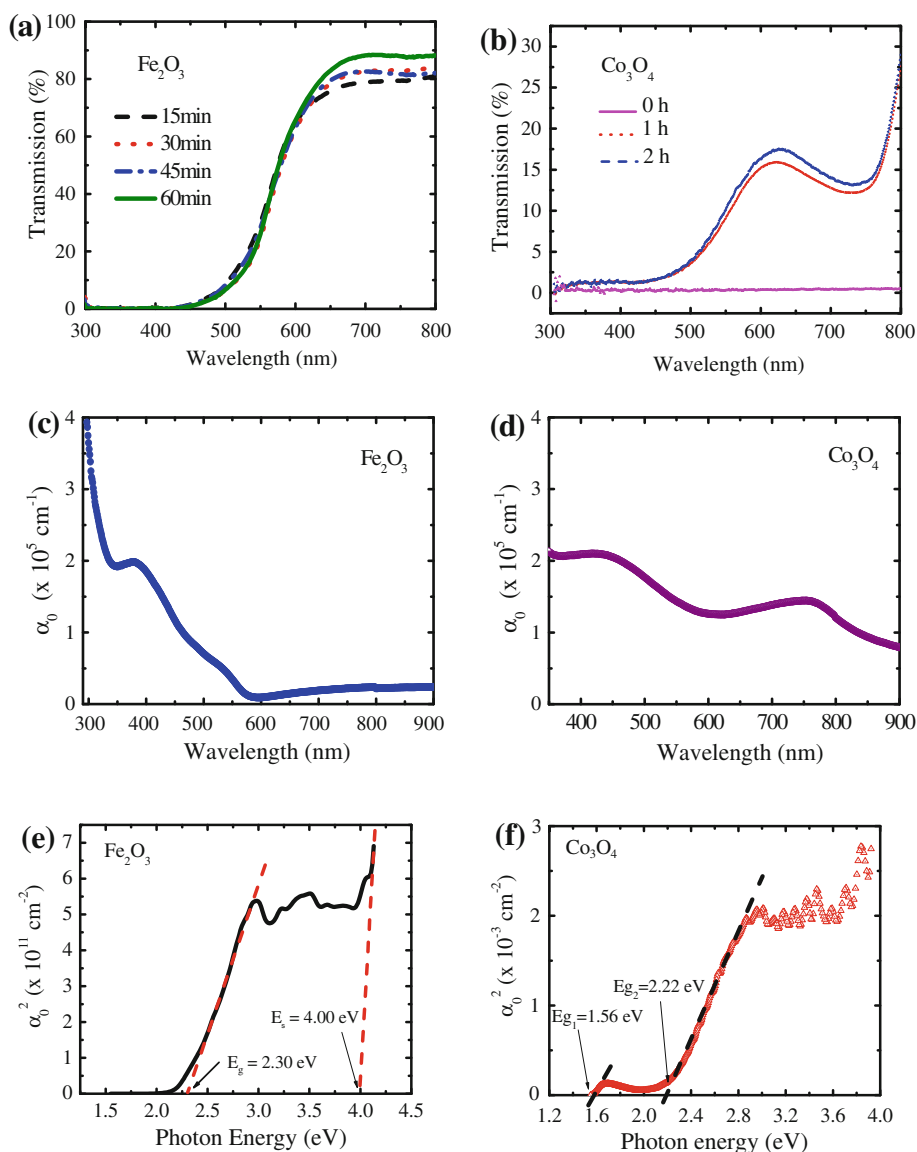


of ≈ 1.56 eV (≈ 798 nm) and another at ≈ 2.22 eV (≈ 561 nm). For a better characterization of our Co_3O_4 samples, we analyzed the power-law dependence of optical transmission spectra of the films as indicated in Fig. 5. It is known that for direct transitions the absorption coefficient should obey the relationship $\alpha_0 \propto (1 - E_g/h\nu)^n$ where E_g is the direct band gap energy, $h\nu$ is the incident photon energy, $n = 1/2$ for direct allowed transitions and $n = 3/2$ for direct forbidden transitions. For indirect transitions we have $\alpha_0 \propto [1 - (E'_g \pm E_p)/h\nu]^n$ where E'_g is the indirect band gap energy, $\pm E_p$ is the energy due to phonon

emission (+) or absorption (−) and n determines the nature of the transition ($n = 2$ for indirect allowed transitions and $n = 3$ for indirect forbidden transitions) [34–36].

Indirect transitions usually occur with phonon participation and typical values of the phonon energies are between 0.01 and 0.02 eV. By analyzing all the possibilities of indirect transitions, we concluded that the exciton energy has also to be considered to understand this case. The logarithm dependence of the optical transmission as a function of the photon energy gives information about the semiconductor exciton energy, E_{ex} , [37] and the obtained value of $E_{\text{ex}} = 1.68$ eV corresponds to a value that allows

Fig. 4 Wavelength dependence of the optical transmittance for different oxidation times **a** α -Fe₂O₃ and **b** Co₃O₄. Absorption coefficient, α_0 , versus wavelength: **c** α -Fe₂O₃, **d** Co₃O₄. The square power-law dependence of α_0 for α -Fe₂O₃ (**e**) and Co₃O₄ (**f**). Films thickness: 200 nm (α -Fe₂O₃); 70 nm (Co₃O₄)



energy match to favor the indirect transition. From these results we could represent the internal band structure of the Co₃O₄ in addition to the one proposed by Thota et al. [38], as shown in Fig. 6. An important conclusion is that one of the allowed indirect transitions is associated with an exciton transition according to the weakly bound electron–hole model (Mott–Wannier exciton). The exciton ionization energy is calculated by using the modified Rydberg equation, $E_{ex} = -(\mu e^4)/(2\epsilon^2 \hbar^2)$ where μ represents the effective mass, e is the electron charge and ϵ is the dielectric function. The electrical permittivity is given by $\epsilon = \epsilon_1 + i\epsilon_2$, where $\epsilon_1 = \epsilon_0[(n_0 + \Delta n)^2 - (k_0 + \Delta k)^2]$ and $\epsilon_2 = \epsilon_0[2(n_0 + \Delta n)(k_0 + \Delta k)]$. Using the experimental values obtained for α_0 and α_2 , presented in Sect. 3.3, we estimated the reduced mass value of $0.19 m_e$, where m_e is the electron mass.

3.3 Nonlinear optical measurements at 800 nm

The NL measurements were performed using the *thermally managed Z-scan (TM-Z scan)* technique [27–30] and the experimental setup is similar to the setup described in [29, 30]. A mode-locked Ti–sapphire laser (800 nm, 150 fs, 76 MHz) was employed. The laser beam was focused on the film by a 10-cm focal length lens and the beam waist at the focal position is 18 μ m. The exposure of the sample to the excitation beam is controlled by a chopper placed inside a telescope introduced in the beam path in such way to minimize the spot size of the beam on the chopper wheel. The measurements are made by acquiring the time evolution of the Z-scan signal for the sample placed in the pre-focal and post-focal positions with respect to the focusing lens. The time resolution of 18 μ s is determined by the chopper opening time ($t = 0$) and the Z-scan signal

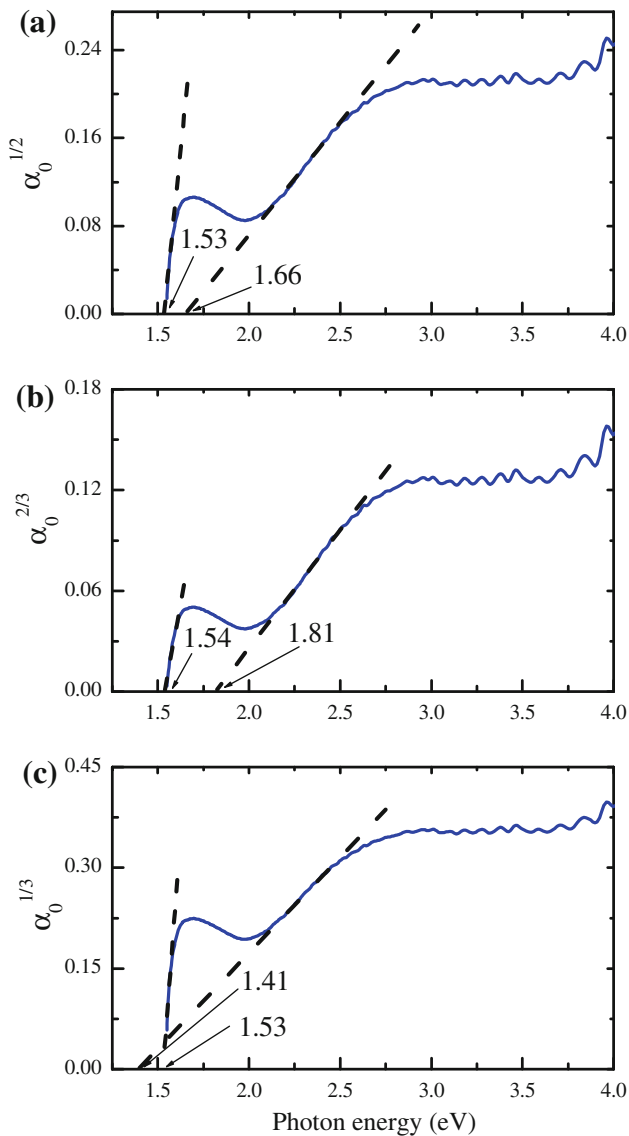


Fig. 5 Data analysis of α_0 to identify direct and indirect transitions

is obtained by delaying the photodetector signal acquisition time with respect to the opening time. From these measurements, the Z-scan curves can be constructed and the contribution of thermal (slow) and nonthermal (fast) nonlinearities can be inferred. Curves representing the transmittance as a function of time (when the sample is in the peak and in the valley positions) are constructed. An exponential curve is used to fit the experimental data and to determine the normalized transmittance free of thermal effects at $t = 0$. Crossing of the two temporal evolution curves corresponding to pre- and post-focal positions indicates the presence of both electronic and cumulative nonlinearities and their relative opposite signs. When the curves corresponding to the rise or decay signals do not cross, we may conclude that the signs of the thermal and

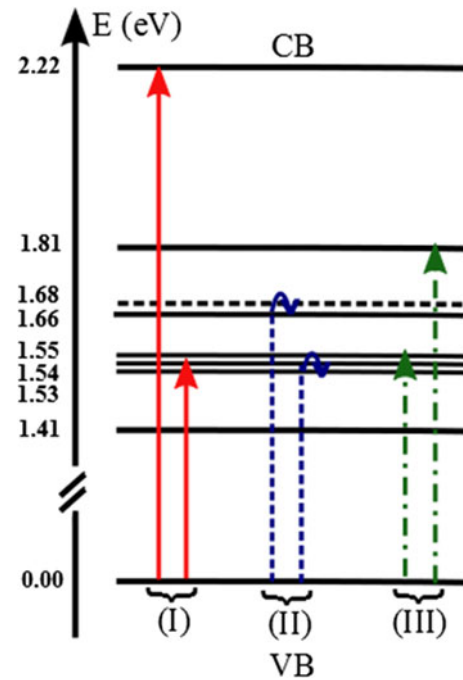


Fig. 6 Intra-bandgap transitions for Co_3O_4 , where (I) represents direct, (II) indirect and (III) forbidden transitions

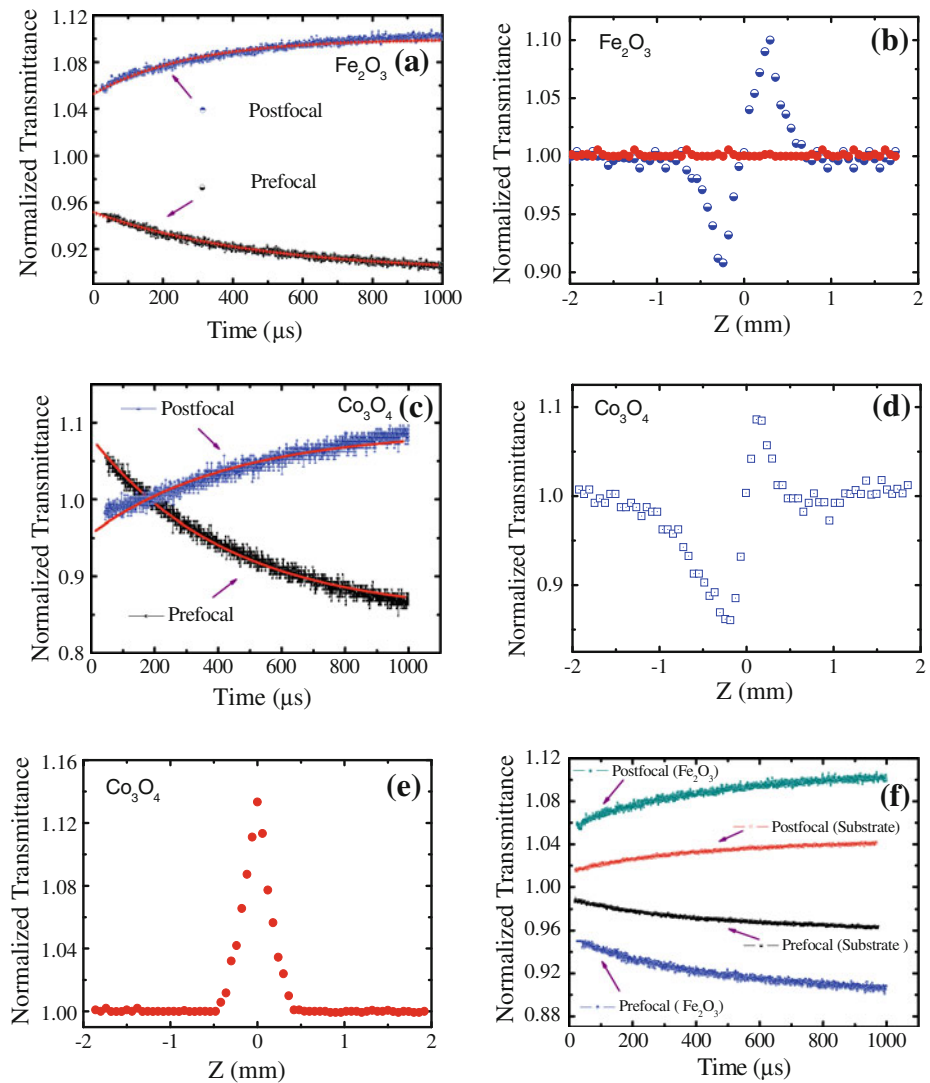
electronic nonlinearities are the same. A flat temporal behavior indicates absence of thermal contributions.

For the *TM-Z scan* measurements we used $\alpha\text{-Fe}_2\text{O}_3$ and Co_3O_4 films with thickness of 200 and 70 nm, respectively. The substrate band gap (≈ 4.0 eV) was determined in a separate linear absorption experiment. We also measured the linear refractive index, n_0 , and found $n_0(\alpha\text{-Fe}_2\text{O}_3) = 2.6044$ and $n_0(\text{Co}_3\text{O}_4) = 2.4791$ at 632.8 nm. The large values of n_0 anticipate large values of the NL refractive index, n_2 , according to the Miller's rule [3].

Figure 7a–f shows the results obtained for both TMO films using laser intensities of 17 GW/cm^2 (for $\alpha\text{-Fe}_2\text{O}_3$) and 5 GW/cm^2 (for Co_3O_4). To make sure that the films are not changing their characteristics due to the laser irradiation, sequential *TM-Z scan* measurements were made in three regimes of laser intensities (low, high, and low intensity). According to [39] this procedure allows evaluation if light-induced damage is occurring in the films. Moreover, in order to identify the NL contribution from the substrate, the *TM-Z scan* measurement was performed in the bare soda-lime glass substrate using the same light intensities as with the TMO samples. The measurements indicate that the NL refractive index of the substrate was $n_2^{\text{sub}} = (5.0 \pm 1.5) \times 10^{-16} \text{ cm}^2/\text{W}$, with negligible NL absorption, in agreement with previous measurements [40].

Figure 7f shows *TM-Z scan* results for the $\alpha\text{-Fe}_2\text{O}_3$ film deposited on soda-lime substrates and for the bare soda-lime glass at $I_0 = 17 \text{ GW/cm}^2$. It is observed that the

Fig. 7 *TM-Z scan* measurements. **a** Time evolution and **b** profile for the α -Fe₂O₃ film ($I_0 = 17$ GW/cm²). **c** Time evolution, **d** closed-aperture Z-scan profile and **e** open-aperture Z-scan profile for the Co₃O₄ film ($I_0 = 5.7$ GW/cm²). The red lines in **a** and **c** correspond to the best numerical fit using the formalism of [28]. **f** Time evolution for the α -Fe₂O₃ film and for the soda-lime glass substrate ($I_0 = 17$ GW/cm²)



substrate exhibits a much smaller NL refractive index than the film which has a thickness $\approx 10^4$ times smaller.

Liquid CS₂ was used as the reference standard for calibration with $n_2 = (2.3 \pm 0.3) \times 10^{-15}$ cm²/W [28] in all experiments.

To determine the NL refractive index of the film, n_2^{film} , we considered the change in the NL phase of the laser field, $\Delta\varphi$, including the substrate contribution through the expression $\Delta\varphi = k_{\text{film}} n_2^{\text{film}} I_0^{\text{film}} L_{\text{eff}}^{\text{film}} + k_{\text{sub}} n_2^{\text{sub}} I_0^{\text{sub}} L_{\text{eff}}^{\text{sub}}$, where I_0^{film} and I_0^{sub} are the laser intensities inside the film and inside the substrate, respectively. The effective thickness of the samples is given by $L_{\text{eff}}^i = [1 - \exp(-\alpha_0^i L^i)] / \alpha_0^i$, where $i = (\text{film}, \text{substrate})$, L^i is the sample thickness and $k_i = 2\pi/\lambda_i$ where λ_i is the wavelength inside the material. Therefore, the NL refractive index of the film is obtained from the expression $n_2^{\text{film}} = \left[\frac{\Delta\varphi_{(t=0)} \lambda}{2\pi n_0^{\text{film}} L_0^{\text{film}}} - \frac{n_0^{\text{sub}} (1-R_2) n_2^{\text{sub}} L_{\text{eff}}^{\text{sub}}}{n_0^{\text{film}}} \right] (L_{\text{eff}}^{\text{film}})^{-1}$, where

$I_0^{\text{film}} = \bar{I}_{\text{film}} (1 - R_1)$, with \bar{I}_{film} being the intensity at the entrance face of the sample and $R_1 = (n_0^{\text{film}} - 1)^2 / (n_0^{\text{film}} + 1)^2$ is the reflectance of the air–film interface. The intensity inside the substrate is given by $I_0^{\text{sub}} = \bar{I}_{\text{sub}} (1 - R_2)$, where $R_2 = (n_0^{\text{film}} - n_0^{\text{sub}})^2 / (n_0^{\text{film}} + n_0^{\text{sub}})^2$ refers to the film–substrate interface. The linear refractive indices of the film and substrate are n_0^{film} and n_0^{sub} , respectively.

The values obtained for the NL refractive indices are: $n_{2(\text{Fe}_2\text{O}_3)} = +(3.9 \pm 1.4) \times 10^{-12}$ cm²/W and $n_{2(\text{Co}_3\text{O}_4)} = -(6.6 \pm 1.2) \times 10^{-11}$ cm²/W.

Figure 7b shows that the NL absorption coefficient of the α -Fe₂O₃ film is smaller than the detection limit of our apparatus that corresponds to 170 cm/GW. On the other hand, the *open-aperture* Z-scan profile for the Co₃O₄ film in Figure 7e shows saturated absorption due to the large

linear absorption of the laser beam that is in resonance with the Co^{2+} band centered at ≈ 760 nm. The saturated absorption coefficient was $\alpha_{2(\text{Co}_3\text{O}_4)} = -(1.5 \pm 0.2) \times 10^4$ cm/GW.

Then, in order to determine the value of $\chi^{(3)}$, we followed the approach of [41], that is valid for samples that present large linear absorption coefficients. In such cases to calculate the values of $\text{Re}\chi^{(3)}$ and $\text{Im}\chi^{(3)}$ we have to consider the results obtained with the *open-* and *closed-aperture* Z-scan configurations and use the expressions:

$$\text{Re}\chi^{(a)}(\text{esu}) = \frac{\text{cn}_0^2}{120\pi^2} \times \left(n_2 - \frac{\alpha_0}{2kn_0} \frac{\alpha_2}{2k} \right), \quad (1)$$

$$\text{Im}\chi^{(a)}(\text{esu}) = \frac{\text{cn}_0^2}{120\pi^2} \times \left(\frac{\alpha_2}{2k} + \frac{\alpha_0}{2kn_0} n_2 \right). \quad (2)$$

Notice that the expressions (1) and (2) reduce to the usual expressions of [42] when the linear absorption is negligible. Observe that due to the term proportional to n_2 in Eq. (2), the value of $\text{Im}\chi^{(3)}$ for the $\alpha\text{-Fe}_2\text{O}_3$ films is not null. On the other hand, the influence of α_0 on the value of $\text{Re}\chi^{(3)}$ is negligible. Therefore, for the Co_3O_4 film, the value of $\text{Im}\chi^{(3)}$ is increased by $\approx 20\%$ while $\text{Re}\chi^{(3)}$ is reduced by $\approx 45\%$ with respect to the values obtained when the usual expressions of [42] are used. The results obtained for the Co_3O_4 film were $\text{Re}\chi^{(3)} = -(5.7 \pm 2.4) \times 10^{-9}$ esu and $\text{Im}\chi^{(3)} = -(1.8 \pm 0.2) \times 10^{-8}$ esu while for the $\alpha\text{-Fe}_2\text{O}_3$ film we determined $\text{Re}\chi^{(3)} = +(6.6 \pm 2.4) \times 10^{-10}$ esu and $\text{Im}\chi^{(3)} = +(2.2 \pm 0.4) \times 10^{-10}$ esu.

4 Summary

In summary, we described in this paper the fabrication of $\alpha\text{-Fe}_2\text{O}_3$ and Co_3O_4 films of good optical quality using a simple oxidation method previously applied for fabrication of NiO films [19]. The electronic third-order optical susceptibility, $\chi^{(3)}$, was measured at 800 nm. The results indicate that the TMO films studied present equally large $|\text{Re}\chi^{(3)}|$ but while $\alpha\text{-Fe}_2\text{O}_3$ presents a self-focusing behavior, the Co_3O_4 film is a self-defocusing material for the wavelength of the experiment. The nonlinear absorption coefficient of $\alpha\text{-Fe}_2\text{O}_3$ is negligible but the Co_3O_4 film shows strong saturated absorption. The positive value of $\text{Im}\chi^{(3)}$ of $\alpha\text{-Fe}_2\text{O}_3$ is small indicating that at 800 nm this material is not a good two-photon absorber although it may be considered for all-optical switching. On the other hand, a negative $\text{Im}\chi^{(3)}$ was determined for the Co_3O_4 film indicating that it may be considered for passive Q-switch due to the large saturated absorption.

References

- C.N.R. Rao, B. Raveau, *Transition Metal Oxides: Structure, Properties, and Synthesis of Ceramic Oxides* (Wiley, New York, 1998)
- R.M. Cornell, U. Schwertmann, *The Iron Oxides, Structure, Properties, Reactions, Occurrence and Uses* (VCH, Weinheim, 1996)
- M. Yamane, Y. Asahara, *Glasses for photonics* (Cambridge University Press, Cambridge, 2000)
- T. He, J. Yao, *Prog. Mater. Sci.* **51**, 810 (2006)
- E.L. Miller, D. Paluselli, B. Marsen, R.E. Rocheleau, *Thin Solid Films* **466**, 307 (2004)
- F. Yubero, M. Ocana, A. Justo, L. Contreras, A. Gonzalez-Elipe, *J. Vac. Sci. Technol. A Vac. Surf. Films* **18**, 2244 (2000)
- Y.J. Park, K.M.A. Sobahan, C.K. Hwangbo, *Surf. Coat. Technol.* **203**, 2642 (2009)
- L. Dghoughi, B. Elidrissi, C. Bernède, M. Addou, M. Alaoui Lamrani, M. Regragui, H. Erguig, *Appl. Surf. Sci.* **253**, 1823 (2006)
- D. Gallant, M. Pézolet, S. Simard, *J. Phys. Chem. B* **110**, 6871 (2006)
- Y.P. He, Y.M. Miao, C.R. Li, S.Q. Wang, L. Cao, S.S. Xie, G.Z. Yang, B.S. Zou, C. Burda, *Phys. Rev. B* **71**, 125411 (2005)
- S. Mitra, S. Das, K. Mandal, S. Chaudhuri, *Nanotechnology* **18**, 275608 (2007)
- S. Thota, A. Kumar, J. Kumar, *Mater. Sci. Eng. B* **164**, 30 (2009)
- R.J. de Oliveira, P. Brown, G.B. Correia, S.E. Rogers, R. Heenan, I. Grillo, A. Galembeck, J. Eastoe, *Langmuir* **27**, 9277 (2011)
- F. Gu, C. Li, Y. Hu, L. Zhang, *J. Cryst. Growth* **304**, 369 (2007)
- M. Ando, K. Kadono, M. Haruta, T. Sakaguchi, M. Miya, *Nature* **374**, 625 (1994)
- T. Hashimoto, T. Yamada, T. Yoko, *J. Appl. Phys.* **80**, 3184 (1996)
- M. Ando, K. Kadono, K. Kamada, K. Ohta, *Thin Solid Films* **446**, 271 (2004)
- H.S. Zhou, A. Mito, D. Kundu, I. Honma, *J. Sol-Gel Sci. Tech.* **19**, 539 (2000)
- R.P. de Melo Jr., B.J.P. da Silva, F.E.P. dos Santos, A. Azevedo, C.B. de Araújo, *J. Appl. Phys.* **106**, 093517 (2009)
- G. Yang, A. Chen, M. Fu, H. Long, P. Lu, *Appl. Phys. A* **104**, 171 (2011)
- H.A. Garcia, G.B. Correia, R.J. de Oliveira, A. Galembeck, C.B. de Araújo, *J. Opt. Soc. Am. B* **29**, 1613 (2012)
- X. Zhu, J. Wang, D. Nguyen, J. Thomas, R.A. Norwood, N. Peyghambarian, *Opt. Mater. Express* **2**, 103 (2012)
- C.P. Singh, K.S. Bindra, G.M. Bhalerao, S.M. Oak, *Opt. Express* **16**, 8440 (2008)
- G. Zotti, G. Schiavon, S.S. Zecchin, *J. Electrochem. Soc.* **145**, 385 (1998)
- K. Široký, J. Jirešová, L. Hudec, *Thin Solid Films* **245**, 211 (1994)
- J.H. Kennedy, D. Dünwald, *J. Electrochem. Soc.* **130**, 2013 (1983)
- M. Falconieri, G. Salvetti, *Appl. Phys. B* **69**, 133 (1999)
- A. Gnoli, L. Razzari, M. Righini, *Opt. Express* **13**, 7976 (2005)
- D. Rativa, R.E. de Araujo, C.B. de Araújo, A.S.L. Gomes, L.R.P. Kassab, *Appl. Phys. Lett.* **90**, 231906 (2007)
- L.A. Gómez, C.B. de Araújo, R. Putvinskis Jr., S.H. Messaddeq, Y. Ledemi, Y. Messaddeq, *Appl. Phys. B* **94**, 499 (2009)
- K. Nagato, M. Furubayashi, T. Hamaguchi, M. Nakao, *J. Vac. Sci. Technol. B* **28**, C6P11 (2010)
- K.J. Kim, Y.R. Park, *Sol. State Commun.* **127**, 25 (2003)
- D. Barreca, C. Massignan, S. Daolio, M. Fabrizio, C. Piccirillo, L. Armelao, E. Tondello, *Chem. Mater.* **13**, 588 (2001)

34. P.S. Patil, L.D. Kadam, C.D. Lokhande, *Thin Solid Films* **272**, 29 (1996)
35. C.S. Cheng, M. Serizawa, H. Sakata, T. Hirayama, *Mater. Chem. Phys.* **53**, 225 (1998)
36. J.I. Pankove, *Optical Process in Semiconductors* (Dover, New York, 1975)
37. C. Kittel, *Introduction to Solid State Physics*, 8th edn. (Wiley, New York, 2004)
38. S. Thota, A. Kumar, J. Kumar, *Mater. Sci. Eng. B* **164**, 30 (2009)
39. K. Fedus, G. Boudebs, C.B. de Araújo, M. Cathelinaud, F. Charpentier, V. Nazabal, *Appl. Phys. Lett.* **94**, 061122 (2009)
40. K. Jamishidi-Ghaleh, N. Mansoor, A. Namdar, *Laser Phys.* **15**, 1714 (2005)
41. R. Coso, J. Solis, *J. Opt. Soc. Am. B* **21**, 640 (2004)
42. M. Sheik-Bahae, A.A. Said, T. Wei, D.J. Hagan, E.W. van Stryland, *IEEE J. Quant. Elec.* **26**, 760 (1990)